Desalination and Water Treatment
www.deswater.com

doi: 10.1080/19443994.2014.940651

55 (2015) 3404–3423
September

Taylor & Francis
Taylor & Francis Group

CFD modelling of profiled-membrane channels for reverse electrodialysis

Luigi Gurreri[a], Michele Ciofalo[b], Andrea Cipollina[a], Alessandro Tamburini[a,*],
Willem Van Baak[c], Giorgio Micale[a]

[a]*Dipartimento di Ingegneria Chimica, Gestionale, Informatica, Meccanica (DICGIM), Università di Palermo (UNIPA), viale delle Scienze Ed.6, 90128 Palermo Italy, Tel. +39 09123863779; email: alessandro.tamburini@unipa.it*
[b]*Dipartimento Energia, Ingegneria dell'Informazione e Modelli Matematici (DEIM), Università di Palermo (UNIPA), viale delle Scienze Ed.6, 90128 Palermo, Italy*
[c]*FUJIFILM Manufacturing Europe BV, Oudenstaart 1, PO Box 90156, 5000LJ Tilburg, The Netherlands*

Received 19 April 2014; Accepted 16 June 2014

ABSTRACT

Reverse electrodialysis (RE) is a promising technology for electric power generation from controlled mixing of two differently concentrated salt solutions, where ion-exchange membranes are adopted for the generation of ionic currents within the system. Channel geometry strongly influences fluid flow and thus crucial phenomena such as pressure drop and concentration polarization. Profiled membranes are an alternative to the more commonly adopted net spacers and offer a number of advantages: avoiding the use of non-conductive and relatively expensive materials, reducing hydraulic losses and increasing the active membrane area. In this work, Computational Fluid Dynamic simulations were performed to predict the fluid flow and mass transfer behaviour in channels with profiled membranes for RE applications. In particular, channels equipped with pillars were simulated. The influence of channel geometry on fluid flow and concentration polarization was assessed by means of a parametric analysis for different profile geometries. The unit cell approach along with periodic boundary conditions was adopted to simulate fully developed boundary conditions. Transport equations, valid also for concentrated solutions, were obtained from the rigorous Stefan–Maxwell equation along with the assumptions of binary electrolyte and local electroneutrality. Simulation results show that, in the geometries investigated here, the pumping power consumption is much lower than in a conventional net spacer and very close to that of the empty channel, while calm zones are generated by the profiles, which may accentuate polarization phenomena.

Keywords: Reverse electrodialysis; Profiled membrane; Concentration polarization; Computational fluid dynamics; Salinity gradient

---

*Corresponding author.

Presented at the Conference on Desalination for the Environment: Clean Water and Energy 11–15 May 2014, Limassol, Cyprus

1. Introduction and literature review

Reverse electrodialysis (RE) is a renewable source for electric power production exploiting the salinity gradient between two solutions at different concentration. The repeating unit of the stack is called *cell pair*. A cell pair comprises of a cationic exchange membrane, a concentrated compartment (e.g. seawater), an anionic exchange membrane and a diluted compartment (e.g. river water). The chemical potential difference between the two solutions generates an electrical potential difference over the ion-exchange membranes (IEMs) that allow the selective transport of ions from the concentrated compartment towards the diluted one. By means of reversible redox reactions at the electrodes, this ionic transport generates an external electric current supplying an external load. More detailed descriptions can be found in the literature [1–5].

Net spacers are usually adopted in RE stacks as mechanical support for the membranes, in order to separate them and create the compartments, as in electrodialysis (ED) stacks. Moreover, the spacer promotes fluid mixing, thus reducing concentration polarization phenomena and consequently enhancing the actual driving force. On the other hand, the adoption of net spacers inevitably presents some drawbacks: increased pressure drop, higher electrical resistance and reduced active membrane area due to spacer shadow effects [2,6–9]. Therefore, the presence of a spacer could even affect negatively the net power, as well as the economical feasibility and competitiveness due to additional costs.

Profiled membranes represent a valid alternative to the traditional net spacers. The profiles, present either on one or on both sides of each membrane, can be obtained by hot pressing and perform the function of spacers separating the membranes and thus generating the channels for the feed solutions, while maintaining good chemical and mechanical characteristics [10]. The use of profiles made by ion-conductive material reduces the ohmic resistance of the stack. Another important advantage is the reduction of the friction factor compared to a spacer-filled channel; this fact allows operating either with lower power consumption for pumping, or at higher Reynolds numbers thus promoting mixing and reducing the residence time. Also, the undesired spacer shadow effect is avoided, and the membrane active area can be increased. Finally, cost savings should not be forgotten.

In the literature, some examples of profiled-membrane applications in electrodialysis experiments can be found. Scott and Lobato [11] carried out limiting current density measurements, and proposed an experimental correlation relating the Sherwood, Reynolds and Schmidt numbers for a cross-corrugated module, valid in the range $Re = 50$–1,000. A flow regime with an irregular flow path was caused by the membrane corrugations (which disturb and break the boundary layers), thereby enhancing mass transfer and providing flow features typical of a turbulent flow [12]. Nikonenko et al. [13] suggested a semi-empirical approach to predict mass transfer characteristics of ED stacks: a higher increase in the mass transfer coefficient due to mixing promotion was obtained for channels with profiled membranes, as compared to spacer-filled channels (and of course, empty channels). In the work of Larchet et al. [14], a stack with profiled membranes exhibited a lower hydraulic resistance and a higher mass transfer rate than a stack with spacer-filled channels. Also, profiled membranes were effective in the overall range of concentrations investigated, while non-conducting spacers were effective only at feed solution concentrations higher than 0.002 M. Balster et al. [15] prepared and characterized a novel membrane design, referred as "membrane with integrated spacer", where the profiles were obtained by capillary forces of a drying polymer solution in contact with a net spacer. This membrane was tested in an ED stack, showing (i) an enhanced mass transfer and (ii) a reduced electrical resistance of the stack compared to the corresponding flat membrane. Strathmann [16] carried out experiments of ED with profiled membranes, obtaining lower stack resistance and higher limiting current densities than in a stack provided with flat membranes and net spacers.

An increasing interest towards the RE technology is noticeable in the recent years, but very few works have been devoted to studying the performance of RE stacks with profiled membranes. As reported in the literature [17], the adoption of ion-conductive spacers improves the system performance in terms of gross power density compared to the use of non-conductive spacers, but of course does not affect the hydraulic loss. First, Brauns [18] proposed the use of profiled membranes for a RE stack. Later, Veerman et al. [6] introduced the concept of "fractal profiled membranes" in order to have short and spacer-less reactor channels. The first real application of profiled membranes to RE is in the experiments by Vermaas et al. [9]. Profiles having a square cross-section arranged and running along the entire channel length were obtained by hot pressing of commercial membranes. The maximum gross power density of the stack with profiled membranes was found to be only slightly larger than that relevant to the stack with net spacers. In fact, although the profiled membranes gave a 30% lower ohmic resistance, they also caused a boundary layer resistance (i.e. concentration polarization) significantly higher due to a poorer mixing promotion. On the other hand, the hydraulic loss was four times lower in the stack with profiled membranes, resulting in a net power density increase of 10%. In another work [7], higher net power densities were theoretically calculated for stacks with profiled membranes compared to stacks equipped with net spacers. Another advantage of profiled membranes is a sensitivity to fouling much lower than that pertaining to stacks with net spacers [19]. Finally, the possibility of adopting profiled membranes with additional sub-corrugations was also investigated [20]; such a configuration did not exhibit a decrease in non-ohmic resistance because the sub-corrugations employed did not act as mixing promoters at the low Reynolds numbers typical of RE systems.

Many studies have been carried out on channels provided with grooves [21–24], and geometries with obstructions, more similar to the profiled membranes, applied for passive micromixers [25–29].

Moreover, several papers can be found in the literature on hydrodynamics and heat transfer predictions via computational fluid dynamics (CFD) in corrugated channels, mainly with reference to heat exchangers [30–34], but very few works have been devoted to mass transfer phenomena in such geometries. Zhang [35] carried out CFD modelling of fluid flow and mass transfer in a cross-corrugated triangular duct by simulating water vapour transport in dry air; correlations of friction factor and Sherwood number with the Reynolds number were proposed. Anyway, to the authors' knowledge, no studies on the CFD modelling of profiled-membrane channels for RE have been presented so far.

On the other hand, CFD is a powerful predictive tool to study the influence of channel geometrical configuration on fluid dynamics, which strongly affects the process performance (net power) by influencing hydraulic friction and concentration polarization phenomena. In the present work, 3D-CFD simulations have been performed to predict fluid flow and mass transfer in channels with profiled membranes for RE stacks. The specific aims of this study are: (i) understanding the behaviour of such geometries with respect to empty channels and spacer-filled channels; (ii) verifying if they can enhance process efficiency and economic competitiveness. In particular, the influence of the channel geometry (shape, size and pitch of profiles) and orientation (fluid flow direction) is assessed via parametric analysis at Reynolds numbers typical of RE applications.

2. CFD modelling

The present CFD simulations are based on the modelling approach described in detail in a previous study [2]. Only the main aspects are reported in this work.

2.1. Systems under investigation

The geometries investigated here consist of channels with membranes provided with profiles on one side, obtainable by hot pressing [9]. The profiles are "pillars" that separate the membranes and create the channels for the feed solutions (Fig. 1).

As schematically shown in Fig. 2, two profile shapes were investigated: (i) square and (ii) circular. The profiles are arranged in a square pitch. The geometrical features of the simulated systems are: (i) the size of the profiles l (edge or diameter), (ii) the distance between two profiles (pitch) L and (iii) the height of the channel h. Corrugated membranes would involve lower pressure drops than spacer-filled channels, allowing eventually the use of thinner channels, which can be a good option to reduce the electrical resistance of the stack; therefore, the present modelling is focused on thin channels of height $h = 160\,\mu\text{m}$. The parametric analysis was carried out on three different values of both profiles' size and pitch: $l = 0.75$, 1.00 and 1.50 mm; $L = 2$, 3 and 4 mm. Also, two different main flow directions were investigated: (i) parallel to one edge of the square pitch of the profiles (flow attack angle $\alpha = 0°$), (ii) along the diagonal of the square pitch (flow attack angle $\alpha = 45°$). The influence of profile shape and flow attack angle was investigated only for $l = 1$ mm and $L = 3$ mm; then, for the circular shape and the flow attack angle of 45°, the influence of l at a fixed value $L = 3$ mm and the influence of L at a fixed value $l = 1$ mm were assessed ($L/l = 2$–4) (see Table 1). For convenience, each case simulated is indicated by an identification code: the first letter indicates the square (s) or circular (c) shape of profiles; then, l, L and α are reported with their respective values. For instance, the case *s-l1-L3-α45* indicates square profile, size $l = 1$ mm, pitch $L = 3$ mm and flow attack angle $\alpha = 45°$.

For comparison purposes, a spacer-filled channel 160 μm thick (Fig. 2(c)) was also simulated. This spacer was made by woven filaments with angle of 90° and mesh length of 462 μm; the fluid attack angle chosen was 45° since such configuration was found to offer performance better than other spacers [2]. Moreover, an empty flat (i.e. spacer-less) channel with the same thickness was simulated as a reference case. The empty channel should be regarded as an ideal

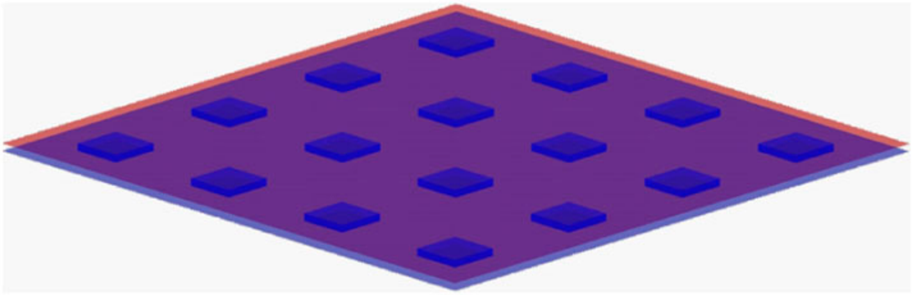

Fig. 1. Sketch of a profiled-membrane channel. Red and blue colours indicate the upper and lower IEMs, respectively. Profiles are obtained from the lower membrane.

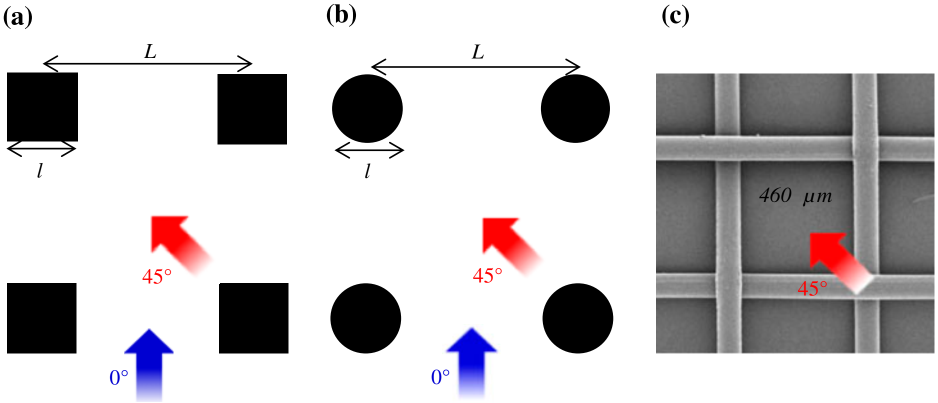

Fig. 2. Sketches of the two profile geometries simulated (a–b). The woven wire spacer is also shown for comparison (c).

Table 1
Profile configurations and Reynolds numbers investigated

Case	Shape	l [mm]	L [mm]	α [°]	Re [–]
s-l1-L3-α0	Square	1	3	0	0.5, 2, 8, 32
s-l1-L3-α45	Square	1	3	45	0.5, 2, 8, 32
c-l1-L3-α0	Circular	1	3	0	0.5, 2, 8, 32
c-l1-L3-α45	Circular	1	3	45	0.5, 2, 8, 32
c-l1-L2-α45	Circular	1	2	45	8
c-l1-L4-α45	Circular	1	4	45	8
c-l0.75-L3-α45	Circular	0.75	3	45	8
c-l1.5-L3-α45	Circular	1.5	3	45	8

condition since a certain "spacer" separating the membranes is compulsory.

The fluid simulated is an aqueous solution of NaCl 0.5 M (typical concentration of seawater) at 25°C, whose physical properties are [36–38]: density $\rho = 1{,}017\ \mathrm{kg/m^3}$, dynamic viscosity $\mu = 9.31 \times 10^{-4}\ \mathrm{Pa\,s}$, diffusivity of NaCl in water $D = 1.472 \times 10^{-9}\ \mathrm{m^2/s}$. Seawater can be adopted in a traditional RE stack as the concentrated feed solution coupled with river water as the diluted one, but a new concept of RE with concentrated solutions, investigated within the EU-FP7 funded REAPower project [39–41], is based on the combination of brine (concentrate) and sea or brackish water (diluate), in order to reduce the stack resistance. Therefore, a solution with seawater concentration may be suitable either as diluted feed or concentrated feed.

2.2. Governing equations

The governing equations for three-dimensional flow of a Newtonian and incompressible fluid are the continuity and the momentum (Navier–Stokes) equations, given by:

$$\vec{\nabla} \cdot \vec{u} = 0 \tag{1}$$

$$\rho \frac{\partial \vec{u}}{\partial t} + \rho \vec{u} \vec{\nabla} \cdot \vec{u} = -\vec{\nabla} \tilde{p} + \mu \nabla^2 \vec{u} + \vec{P} \tag{2}$$

where $\vec{u}$ is the velocity, ρ is the density, μ is the dynamic viscosity, $\tilde{p}$ is the periodic component of pressure and $\vec{P}$ is the body force per unit volume. This last term has same effect of the large-scale component of the driving pressure gradient along the main flow direction [2,42].

The flow regime was predicted to be steady even at the highest Reynolds number investigated in preliminary time-dependent simulations, thus only steady-state simulations were carried out. The density was assumed to be constant since its changes associated with streamwise and cross-stream concentration gradients were estimated to be very small. For the same reason, buoyancy, due to the concentration gradients, was neglected.

As explained in the following section, the computational domain consists of a repetitive periodic unit of the channel. In order to impose periodic boundary conditions also for the electrolyte concentration C, notwithstanding the streamwise variation of the bulk concentration, a *periodic concentration* $\tilde{C}$ was defined as:

$$\tilde{C}(x, y, z) = C(x, y, z) - ks \tag{3}$$

where s is the abscissa along the flow direction and k is the concentration gradient along s due to the flux in or out of the walls:

$$k = \frac{\bar{J}^{d}_{IEM} \cdot S}{u_{s,ave} \cdot V} \tag{4}$$

where $\bar{J}^{d}_{IEM}$ is the mean value of the electrolyte flux entering the channel at walls (imposed in the simulation), S is the membrane surface area in a unit cell, $u_{s,ave}$ is the volume-averaged velocity along s in the unit cell and V is the unit cell volume. As demonstrated in [2], a transport equation for the electrolyte concentration, valid also for concentrated solutions, can be obtained from the rigorous Stefan–Maxwell equation under the assumptions of (i) binary electrolyte and (ii) local electroneutrality

$$\vec{\nabla}\left(\tilde{C}\vec{u}\right) = \vec{\nabla}\left[D \frac{b}{b + (a - M_e)\left(\tilde{C} + ks\right)} \vec{\nabla}\tilde{C}\right] - ku_s \tag{5}$$

where D is the diffusion coefficient of the electrolyte, a and b are the linear regression parameters of the function $\rho = \rho\ (C)$ [36], M_e is the molar mass of the electrolyte and u_s is the local value of the velocity component along the main fluid flow direction s. Note that Eq. (5) is written for the periodic component $\tilde{C}$ of concentration. The real (non periodic) concentration C can be inferred from $\tilde{C}$ using Eq. (3).

Eq. (5) appears as a convection–diffusion equation, where there is a non-linearity in the diffusive term and the additional term ($-ku_s$) arises from the definition of the periodic concentration. As demonstrated [2], the migrative term (divergence of the migrative flux) is negligible compared to the diffusive one and it does not affect appreciably the concentration field; hence, the migrative term is not included in Eq. (5). Note that this does not imply that migrative fluxes are negligible, only that they are superimposed with the diffusive ones without affecting them and are reflected in the boundary conditions of Eq. (5).

2.3. Computational domains and boundary conditions

A single channel was simulated in the CFD simulations. The electrolyte flux at the walls (representing the membrane–solution interfaces) is imposed to be in-going, i.e. the channel simulated represents the dilute compartment. However, once properly normalized, the results have general validity in order to assess concentration polarization phenomena in terms of concentration change from the bulk to the walls. The computational domain does not include the membranes and the modelling does not take into account phenomena at molecular scale occurring in the electric double layer in the membrane–solution interface.

Fully developed flow and concentration fields are assumed, so that is possible to simulate the elementary geometric domain representing the periodic unit of the channel (unit cell). Many CFD studies can be found in the literature on spacer-filled channels [2,42–47] and corrugated channels [30,31,33,35] based on this approach, because the fully developed flow condition is attained after just a few unit cells [48].

The unit cell for the profiled-membrane channels was built up by joining the centres of four profiles (see Fig. 3(a)). A totally equivalent domain would be

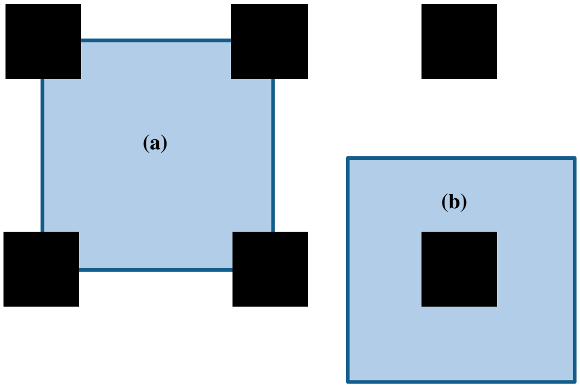

Fig. 3. Possible equivalent unit cells. Type (a) was chosen in the present work.

that indicated in Fig. 3(b). Fig. 4 shows an example of unit cell chosen for the two profile shapes and for the spacer-filled channel investigated in the present work.

Multi-block hexahedral grids were used since they allow a higher accuracy and facilitate grid independence assessment [42]. The size of the computational cells employed along the thickness of the channel (i.e. $h = 160\ \mu m$) was chosen to be the half of the sizes imposed along the other two directions thus resulting into a grid much finer in the direction perpendicular to the membranes. A refinement was also set towards these walls. A grid independence analysis was performed and the parametrical study was conducted using grids still providing grid independent results. More precisely, various grids were tested, generated by setting a number of divisions of the channel thickness ranging from 10 to 60; the comparison of global quantities (average values) and local quantities (profiles on lines perpendicular to the walls) established a grid independence of results for meshes with a minimum number of divisions of the thickness equal to 30 (vertical element size equal to 5.33 μm). Therefore, this size was chosen for carrying out all the simulations reported in the present paper. It results into grids with a number of computational cells ranging from $\sim 1 \times 10^6$ to $\sim 4 \times 10^6$ depending on the specific pitch to height ratio. A hybrid hexahedral–tetrahedral grid was generated for the case of the spacer-filled channel ($\sim 1.6 \times 10^6$ of computational cells) as described in detail elsewhere [2,42,47]. Fig. 5 shows enlarged details of meshes employed for two profiled-membrane channels and for the spacer-filled channel.

Translational periodicity conditions were imposed on the lateral boundaries of the domain, apart from the interfaces fluid–membrane profile. The unit cell orientation was kept fixed in all cases with respect to the *Oxyz* frame so that the main flow direction *s* was along the *z*-axis in the case of flow attack angle $\alpha = 0^\circ$, and along the bisecting of the *x*- and *z*-axes for $\alpha = 45^\circ$ (see Fig. 4). The body force per unit volume $\vec{P}$ was set in order to achieve a range of Reynolds numbers between 0.5 and 32. The maximum value investigated is relatively high for this kind of applications; the corresponding fluid velocity is around 0.1 m/s. However, an important feature of profiled-membrane channels is a lower friction factor, which allows operating at higher Reynolds numbers compared to those typical of spacer-filled channels.

All the other boundaries representing the fluid–membrane interface are set as walls with no-slip conditions. A Neumann boundary condition was set for the concentration: a uniform diffusive flux is imposed at the upper and lower walls, while the flux is set to zero at the lateral walls (fluid–membrane profile interfaces). The latter assumption was done considering that an ion close to the membrane profile would cross solution and membrane more easily than profile and membrane, especially for highly conductive solutions and profiles with a high *l*/*h* ratio. Furthermore, the ionic current across the membrane profiles is expected to be so low due to their small area, that its contribution to the overall current is negligible.

Assuming the hypothesis of ideal membranes (permselectivity equal to 100%) and transport numbers

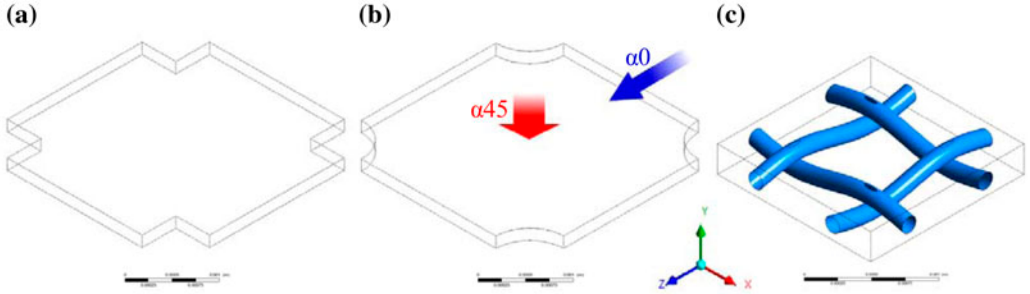

Fig. 4. Unit cell geometry for (a) *s-l1-L3* channel, (b) *c-l1-L3* channel and (c) spacer-filled channel.

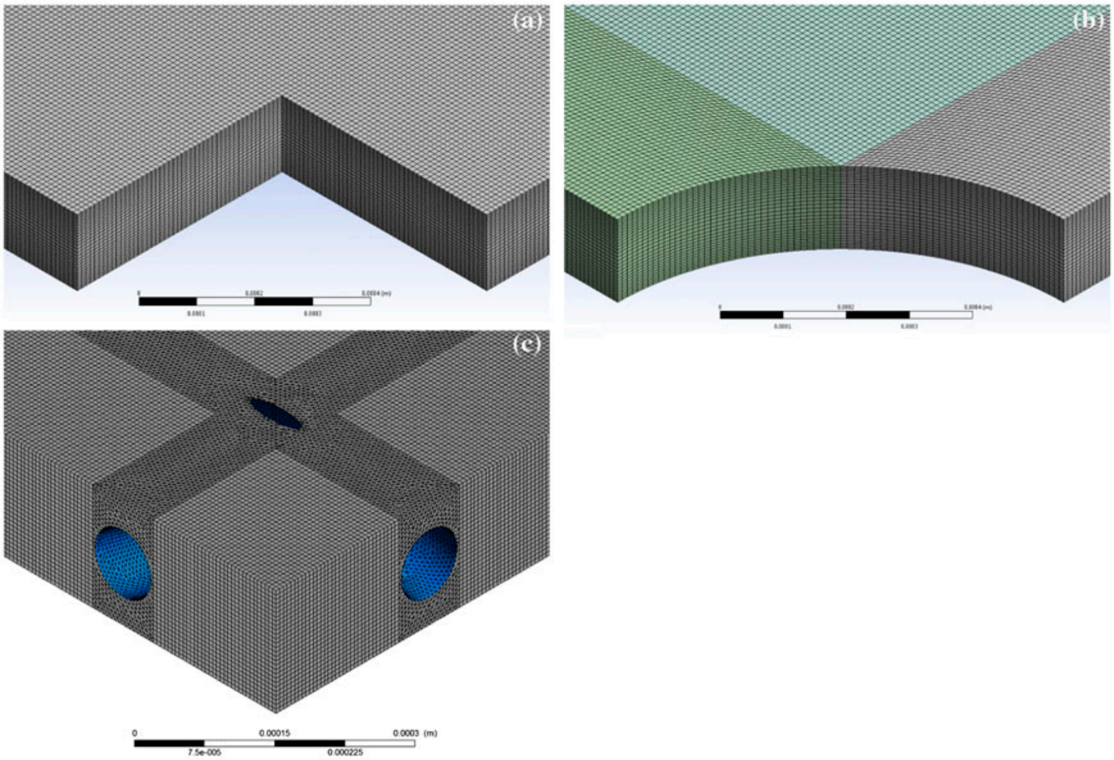

Fig. 5. Discretization of the unit cell for (a) *s-l1-L3* channel, (b) *c-l1-L3* channel and (c) spacer-filled channel.

of ions in solution equal to 0.5, the diffusive flux at the membranes J^d_{IEM} can be correlated to the current density i [2] as

$$J^d_{IEM} = \frac{i \cdot 0.5}{F} \tag{6}$$

where F is the Faraday constant (96,485 C/mol). A uniform current density of 200 A/m^2 (over the total area) was imposed, a provisional high value achievable in systems optimized for high power density by the use of highly conductive solutions and membranes. Therefore, polarization phenomena are evaluated in conditions where they could be the limiting factor for the process performance. Eq. (5) includes the concentration in the diffusivity correction term, thus resulting in a flux that is not linearly dependent on the concentration gradient. However, the non-linearity of the transport equation is so small [2], that simulating different values of the current density is not needed.

2.4. Definitions

The hydraulic diameter of the channel is defined as in the case of an empty (spacer-less) channel of infinite streamwise and spanwise extend

$$d_{h,void} = 2h \tag{7}$$

The Reynolds number was calculated in accordance with [2,49]

$$Re = \frac{\rho\, u_{s,void} d_{h,void}}{\mu} \tag{8}$$

where $u_{s,void}$ is the average velocity along the main flow direction s in a corresponding spacer-less channel, i.e. the ratio between flow rate and cross-sectional area of the empty channel.

The Fanning friction factor is defined as

$$f = \frac{\Delta p}{\Delta s} \frac{d_{h,void}}{2\rho u^2_{s,void}} \tag{9}$$

where $\Delta p/\Delta s$ is the mean pressure gradient along the flow direction s and coincides with the module of the source term $\vec{P}$ in Eq. (2). The pumping power consumption is evaluated by means of the dimensionless power number, defined as [50]

$$Pn = \mathrm{SPC}\frac{\rho^2 h^4}{\mu^3} = \frac{1}{8} f\, Re^3 \tag{10}$$

where SPC is the specific power consumption per unit volume

$$\mathrm{SPC} = \frac{\Delta p}{\Delta s} u_{s,void} \tag{11}$$

Mass transfer performance of RE channels can be suitably assessed by the *polarization factor*. For the diluted channel of a cell pair, this can be defined either as a local wall quantity

$$\theta = \frac{\hat{C}_b}{C_w} \tag{12}$$

where C_w is the local concentration at the membrane–solution interfaces (upper and lower walls), and $\hat{C}_b$ is the bulk concentration, defined as the mass flow weighted average of the concentration on a plane perpendicular to the main flow direction s and placed midway along the unit cell, or as an average quantity

$$\theta_{ave} = \frac{\hat{C}_b}{\overline{C}_w} \tag{13}$$

where $\overline{C}_w$ is the averaged wall concentration. Note that θ_{ave} does not coincide with the mean value of the local θ over a wall. The maximum value of the average polarization factor θ_{ave} is 1 and represents the condition of absence of polarization. For the concentrated channel of the cell pair, the definition of θ and θ_{ave} must be reversed; in this case, θ_{ave} coincides with the mean value of θ over a wall.

θ_{ave} quantifies polarization phenomena effects: the actual driving force of the system is reduced by a voltage drop due to the concentration polarization in the boundary layers [7]; this loss can be calculated as the logarithm of the product of the polarization factors in the two channels of a cell pair [2], which, on the basis of the above definitions, is always < 1.

2.5. Computational details

The continuity, momentum and mass transport equations (Eqs. (1), (2), (5)) were discretized and solved in the computational domain with the boundary conditions described in Section 2.3 by means of the finite volume code Ansys®-CFX 14. As the initial guess, zero velocity and a homogeneous value of the periodic concentration (0.5 M) were imposed. The *High Resolution* scheme was used for the advection terms and shape functions were used for the spatial derivatives of the diffusion terms. A coupled algorithm was adopted to solve for pressure and velocity. All simulations were run in double precision. Convergence was attained after a different number of iterations depending on the specific simulation but in all cases, the convergence criteria were the achievement of stabilized values at the monitor points along with residuals lower than 1.0e-10. The simulations were carried out by a double-hexacore workstation with 2.6 GHz CPU and 64 GB RAM, and typically required some hours each.

3. Results and discussion

In this section, simulation results are presented and discussed by analyzing the effect of geometric parameters and fluid dynamic conditions on fluid flow and mass transfer. In Section 3.1 the effect of profile shape, flow attack angle and Reynolds number is investigated for $l = 1$ mm and $L = 3$ mm (cases *l1-L3*). Then, in Section 3.2, the parametrical analysis is focused on the effect of profile size l and pitch L, while the other parameters are kept fixed; in particular, for the circular shape, the flow attack angle *α45* and $Re = 8$, the effect of three values of l (*l0.75*, *l1* and *l1.5*) for the pitch *L3* and three values of L (*L2*, *L3* and *L4*) for the size *l1* is assessed, so that the ratios $L/l = 2$–4 are investigated (see Table 1).

3.1. Influence of profile shape, flow attack angle and Reynolds number

3.1.1. Velocity and concentration fields

Fig. 6 reports contour plots of the streamwise velocity component u_s (normalized by $u_{s,ave}$) on a x–z plane placed at mid-height, for cases *l1-L3* at $Re = 8$ ($u_{s,void} \approx 2.3$ cm/s, a typical value for RE channels). The profiles are full-thickness obstacles which influence the fluid motion so that the flow field deviates significantly from that relevant to a corresponding empty channel. Clearly, the absence of velocity components perpendicular to the membranes is a prominent feature of profiled-membrane channels. The cross-section of the channel is periodically reduced by the obstacles, thus resulting in a velocity increase between two profiles, especially close to the obstacles themselves. At the same time, low-velocity wake zones can be recognized both downstream of each obstacle and in the stagnation areas just upstream of the next obstacle. This is more evident for the *α0* cases. Circular shaped obstacles provide a velocity distribution more uniform than square obstacles due to the lack of sharp edges. The velocity field is characterized by a saddle shape strongly influenced by the attack angle. For the *α0* cases, in the central part of the

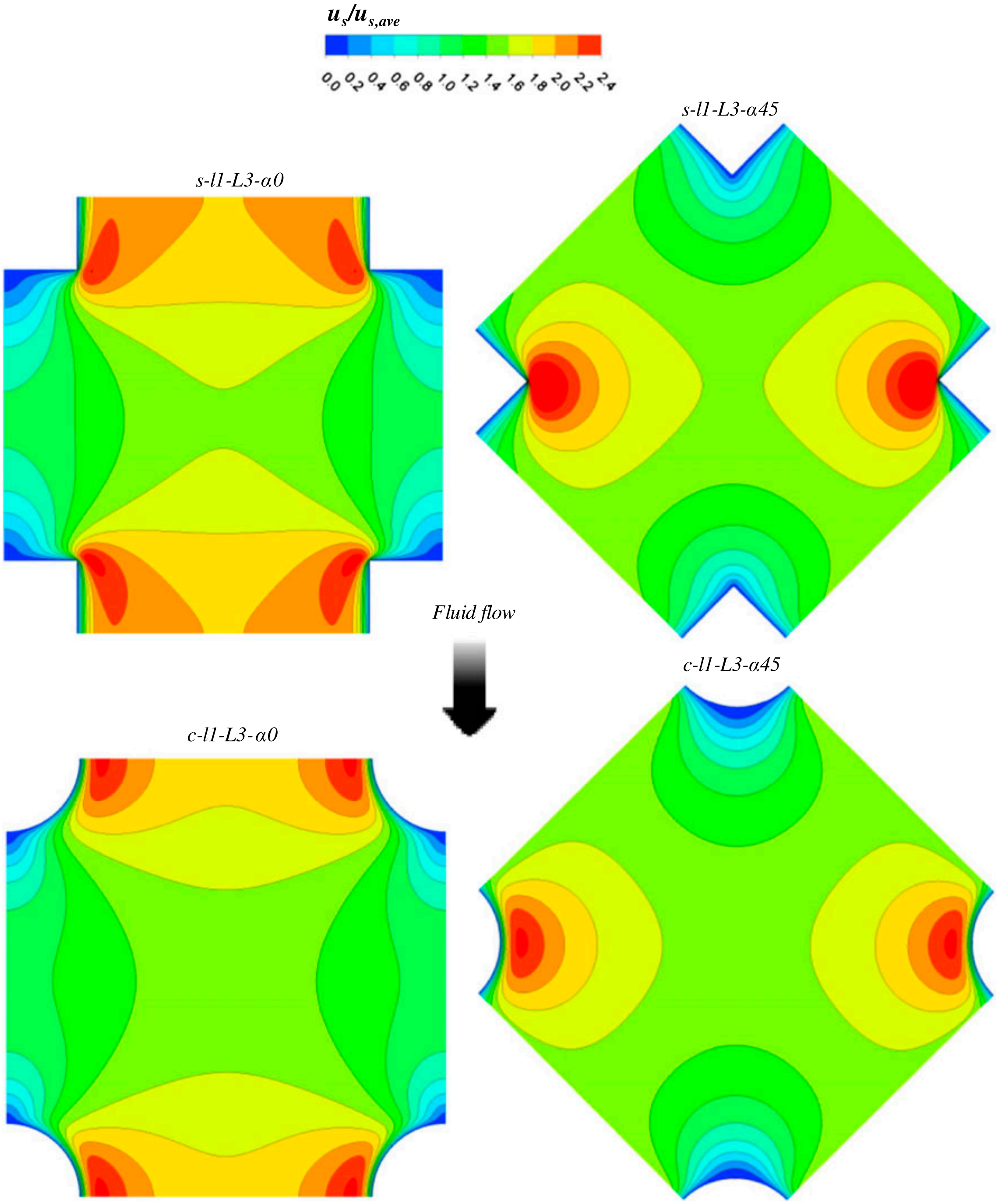

Fig. 6. Maps of the normalized streamwise velocity component on the *x–z* midplane for *s-l1-L3-α0*, *s-l1-L3-α45*, *c-l1-L3-α0* and *c-l1-L3-α45* channels at $Re = 8$.

unit cell, there is a minimum along the flow direction and a maximum in the direction perpendicular to it, while this feature is inverted for the *α45* cases.

The streamlines are affected by the obstacles and follow their boundary in the region close to them, as highlighted by the velocity vector plots in Fig. 7. No flow separation is observed, which indicates the presence of a creeping flow regime.

Fig. 8 reports maps of the local polarization factor $\theta = \hat{C}_b \big/ C_w$ on one of the walls for the same cases of Figs. 6 and 7. In the *α0* cases, the θ distribution is highly non uniform. The lowest θ values correspond

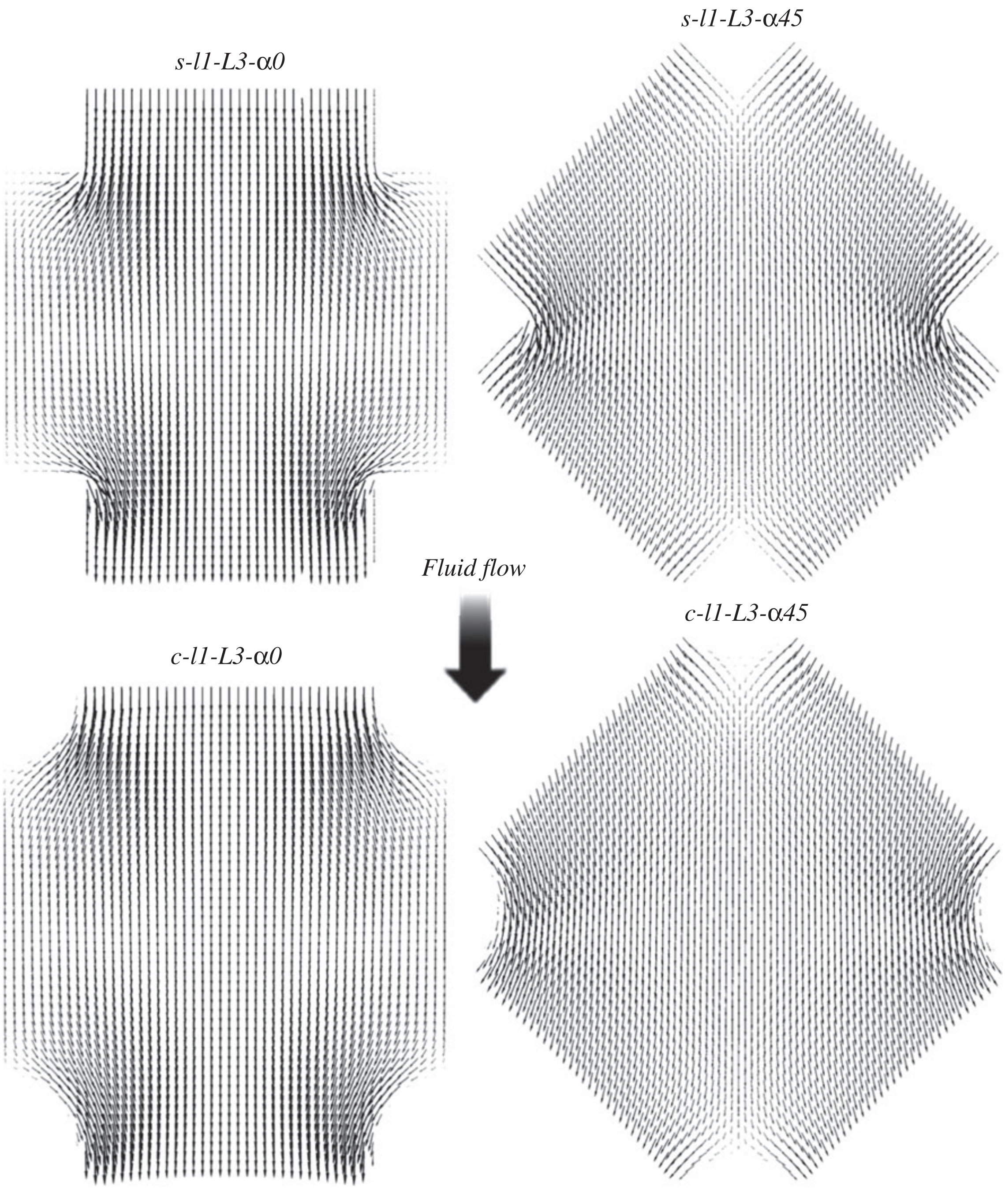

Fig. 7. Velocity vector plots on the x–z midplane for *s-l1-L3-α0*, *s-l1-L3-α45*, *c-l1-L3-α0* and *c-l1-L3-α45* channels at $Re = 8$.

to regions of high wall concentration, associated with low mass transfer coefficients, and are observed in the calm regions between two profiles along the main flow direction and all around the profiles. On the contrary, high θ values are observed in the central region; note that local values of $\theta > 1$ are compatible with $\theta_{ave} < 1$. The case *α45* results in a much more homogeneous distribution of concentration, leading to higher average polarization factors (i.e. less polarization effects).

In order to show how the flow dynamics conditions affect concentration polarization, Fig. 9 reports concentration profiles in the direction perpendicular to the membranes for cases *c-l1-L3-α0* (a) and *c-l1-L3-α45* (b) at various *Re*. The concentration is averaged in each plane parallel to the walls and normalized by its

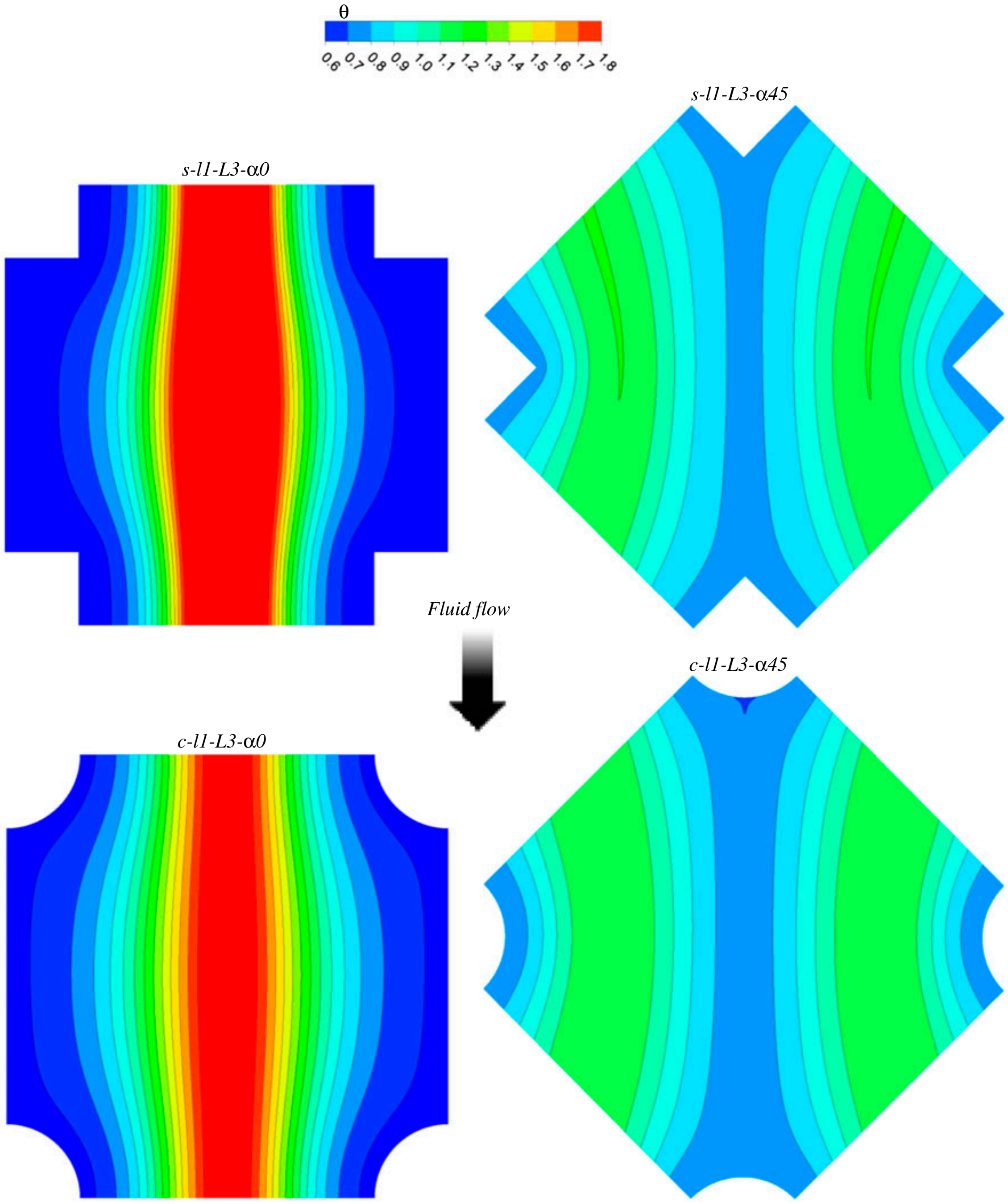

Fig. 8. Maps of the local polarization factor $\theta = \hat{C}_b \Big/ C_w$ on one of the fluid–membrane interfaces for *s-l1-L3-α0*, *s-l1-L3-α45*, *c-l1-L3-α0* and *c-l1-L3-α45* channels at $Re = 8$.

bulk value. Notwithstanding the absence of a velocity component perpendicular to the walls, a significant reduction of the normalized mean concentration at the walls (i.e. a significant increase of $\theta_{ave} = \hat{C}_b \Big/ \overline{C}_w$) is obtained at higher *Re*. The influence of *Re* is more evident for $\alpha = 0^\circ$. For low *Re*, the lowest $\overline{C}_w$ values (i.e. highest θ_{ave} values) are obtained for $\alpha = 45^\circ$, while for the highest *Re* (32), the distributions are very similar for the two angles. The same profiles are practically obtained at $Re = 0.5$ and $Re = 2$ due to self-similar creeping flow distributions at very low Reynolds numbers. For higher *Re*, the curve shape varies because of

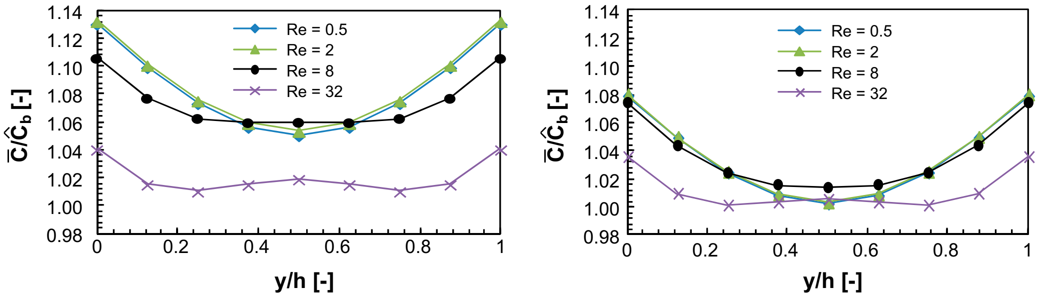

Fig. 9. Normalized area-averaged electrolyte concentration in the direction perpendicular to the membrane–solution interfaces at various *Re* for channels (a) *c-l1-L3-α0* and (b) *c-l1-L3-α45*.

the lack in self-similarity of the fluid flow and concentration fields caused by the presence of the profiles within the channel [2,42]. Note that, in Fig. 9, concentration values are simple area averages and are everywhere larger than the bulk concentration, which is a mass flow average, due to the influence of low-speed, high-concentration regions; as expected from the velocity maps in Fig. 6, this effect is much more evident for $\alpha = 0^\circ$ and low Reynolds numbers.

3.1.2. Global parameters

In Fig. 10, the Fanning friction factor (see Eq. (9)) is reported as a function of the Reynolds number for the *l1-L3* cases. f is normalized with respect to that in an empty channel ($24/Re$). Unlike net spacers, the membrane profiles investigated here lead only to slight increments of pressure drops with respect to the empty channel, mainly due to the associated area restriction. It is worth noting that the flow attack angle has practically no effect for the circular shape and only a small effect, limited to the highest *Re*, for the square shape, notwithstanding it affects heavily the flow field (see Figs. 6 and 7). This means that, especially for the circular profile shape, overall pressure drop is the sum of the individual pressure drops across each obstacle and thus depends only on the number of obstacles per unit area, which, of course, does not depend on the flow attack angle. On the contrary, the obstacle shape has a more significant influence; the square shape implies a friction factor ~8% higher than the circular one. Note that, in the present range of *Re*, the friction factor for the net spacer-filled channel is ~6 times higher than that the empty channel. Up to $Re \approx 10$, the friction factor for the profiled geometries can be interpolated by power functions as

$$f = A\,Re^{-1} \tag{14}$$

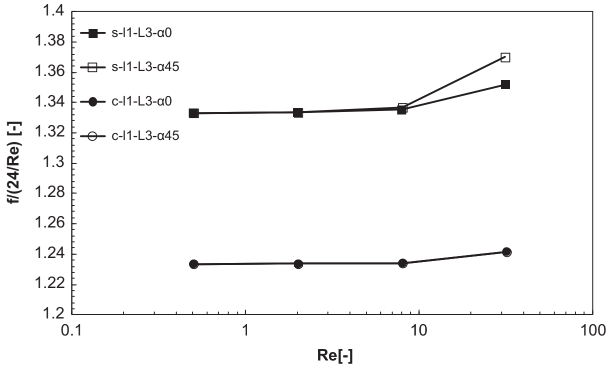

Fig. 10. Fanning friction factor normalized by that pertaining to an empty channel ($24/Re$) as a function of the Reynolds number for *l1-L3* profile configurations.

For the empty channel, $A = 24$. For the profiled-membrane channels, $A \approx 29.6$ (circular obstacles) and $A \approx 32.0$ (square obstacles). At higher *Re*, the exponent in Eq. (14) begins to deviate from −1, since the obstacles induce slight but increasing inertial effects, generating flow fields which do not remain self-similar as *Re* increases.

The pumping power consumption represents a fundamental factor affecting the process efficiency as it determines the net power producible by the stack. Therefore, a more effective comparison of RE channels can be done by considering the dimensionless power number *Pn*, defined in Eq. (10). This quantity is reported in Fig. 11 as a function of the Reynolds number for (i) *l1-L3* cases, (ii) empty and (iii) spacer-filled channels.

The relationship *Pn–Re* can be expressed by an equation in the form

$$Pn = B\,Re^{m} \tag{15}$$

where $B = A/8$ and $m \approx 2$. Compared to the empty channel, the profiled-membrane channels provide an increment in *Pn* of about 23 and 33%, respectively, for the circular and square shape, while the spacer-filled channel requires a pumping power increase of ~5.7 times. The square shape requires a pumping power about 8% larger than the circular shape. Notably, the flow attack angle is irrelevant for the profiled-membrane channels as discussed above with regard to *f*.

The results obtained regarding the average polarization factor defined in Eq. (13) are reported in Fig. 12 which shows θ_{ave} as a function of *Re* for the cases *l1-L3*. Clearly, due to geometric symmetry and imposed equal fluxes, θ_{ave} values for upper and lower walls are equal. In the empty channel, self-similar parallel flow is present at all *Re*, thus resulting in a θ_{ave} value independent of the Reynolds number. In the profiled-membrane channels, a significant increase of θ_{ave} can be observed as *Re* increases beyond ~4 (creeping flow regimes), due to the increased inertial fluid flow phenomena favouring a mass transfer enhancement.

It is worth observing that profiled-membrane channels offer performance even worse than the empty channel at low *Re*. This is due to the regions of high polarization (low θ) which arise streamwise between two profiles and around the profiles, as discussed above (Fig. 8). At higher *Re*, the mean polarization factor is higher for the profiled-membrane channels. Analogous considerations can be inferred by plotting θ_{ave} against the power number Pn (Fig. 13): there exists a cut-off value of *Pn*, depending on the specific profiled geometry, beyond which profiled membranes become more efficient than the empty channel.

In the range of *Re* investigated, the spacer-filled channel simulated here is the configuration yielding the maximum θ_{ave}. A large mass transfer enhancement is obtained because the woven arrangement of the spacer wires gives the fluid significant velocity components perpendicular to the walls, whose relative importance increases as the flow rate increases. Moreover, the flow attack angle *α45* avoids the presence of stagnant zones.

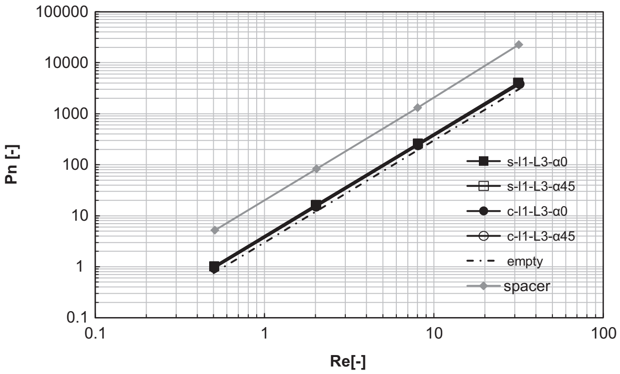

Fig. 11. Dimensionless power number as a function of Reynolds number for *l1–L3*, empty and spacer-filled channels.

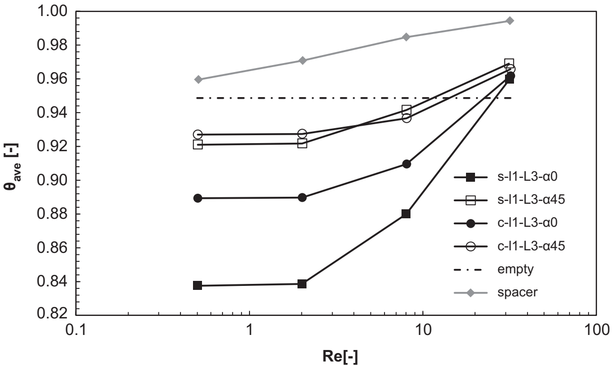

Fig. 12. Average polarization factor θ_{ave} as a function of the Reynolds number for *l1–L3*, empty and spacer-filled channels.

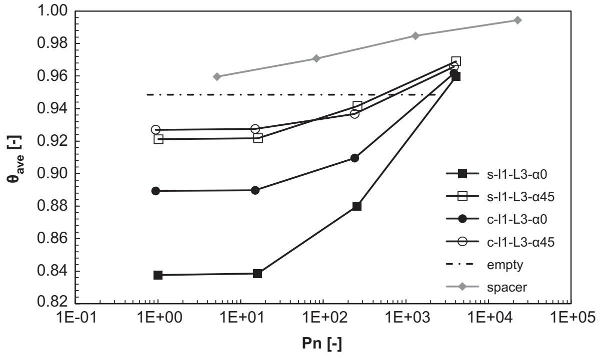

Fig. 13. Average polarization factor θ_{ave} as a function of the dimensionless power number for *l1–L3*, empty and spacer-filled channels.

By comparing the different profile configurations considered in Figs. 12 and 13, it can be observed that the flow attack angle affects significantly mass transport, although it has only slight effects on pressure losses. As highlighted above, high polarization regions occur within the system for the case *α0*, thus leading to a lower θ_{ave}. The shape of the profiles seems to affect polarization phenomena more in the case *α0*, where the circular shape allows a higher θ_{ave}; on the contrary, very similar θ_{ave} values are obtained for the two shapes in the case *α45*. However, at high *Re,* all the configurations provide a similar performance.

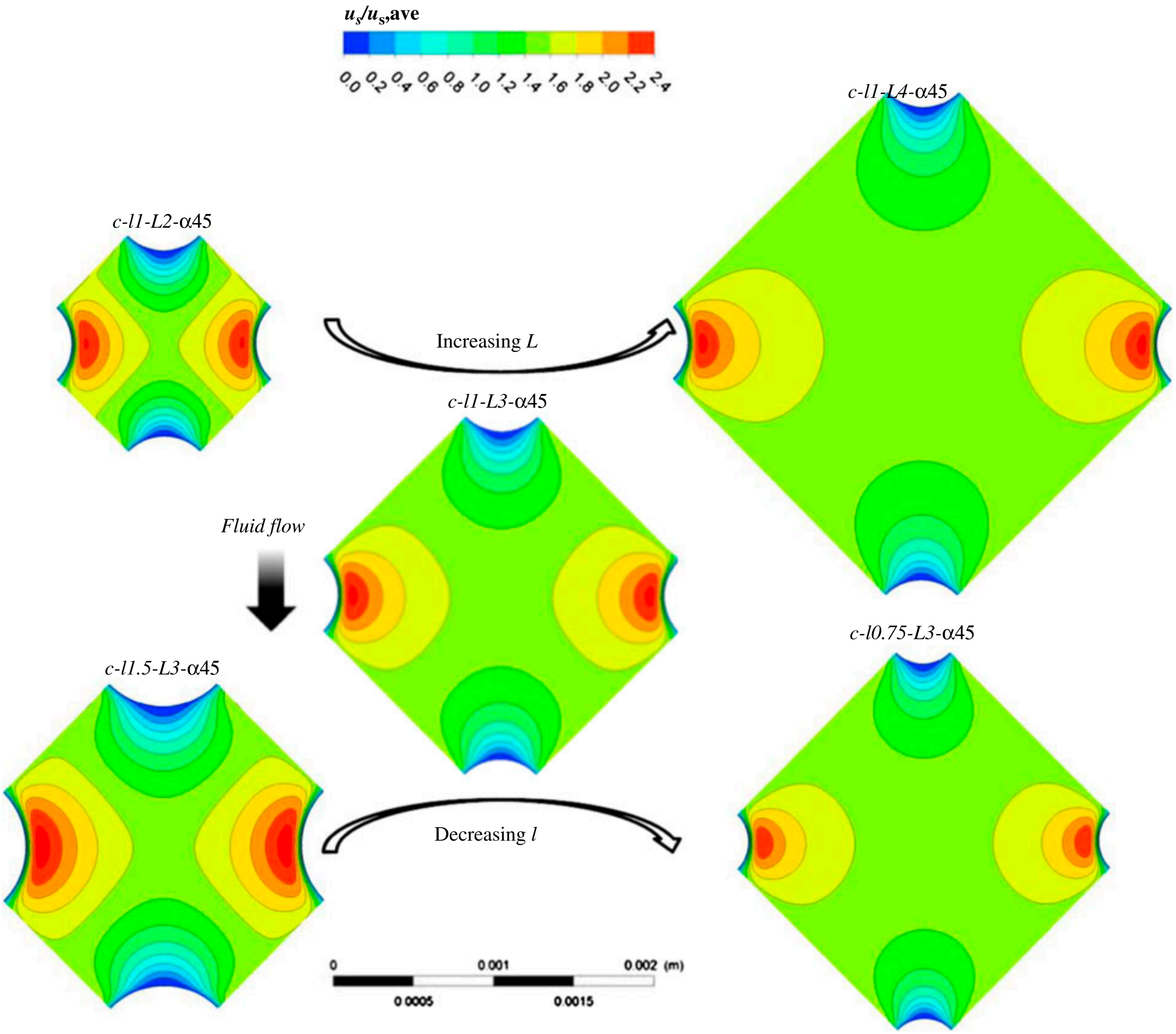

Fig. 14. Maps of the normalized streamwise velocity component on the x–z midplane for *c-l1-L2-α45*, *c-l1-L4-α45*, *l1–L3-α45*, *l1.5-L3-α45* and *l0.75-L3-α45* channels at $Re = 8$.

Therefore, channel geometry and orientation might have a significant effect on polarization phenomena, but their relative importance depends on the flow rate.

3.2. Influence of size and pitch

3.2.1. Velocity and concentration fields

In this section, the effects of the size l and pitch L of the profiles is analysed ($L/l = 2, 3, 4$). For simplicity, the comparison is restricted to the circular shape, the flow attack angle $\alpha 45$ at $Re = 8$. Figs. 14 and 15 show normalized streamwise velocity maps and corresponding vector plots on an x–z plane placed at mid-height. Note that all configurations are represented to the same geometrical scale. At the fixed value of the size *l1*, by increasing L, the effects are: (i) a more homogeneous velocity field, i.e. a larger portion of the plane exhibits velocities close to the average; and (ii) velocity vectors more aligned to the main flow direction s, i.e. a less tortuous flow path. Similarly, at the fixed value of the pitch *L3*, the reduction of l provides practically the same effects. Summarizing, similar flow fields are found for the geometries with the same L/l ratio (*l1-L2* with *l1.5-L3* and *l1-L4* with *l0.75-L3*). This shows that the influence of the L/h or l/h ratios is only minor.

The local polarization factor θ on one of the walls is reported in Fig. 16. Note that the scale of θ in this figure was kept equal to that adopted in Fig. 8

although the present variation range is much more limited. Therefore, the central map in Fig. 16 is identical to that reported in Fig. 8 for the same configuration (*c-l1-L3-α45*). As L increases, a slightly less uniform distribution of θ is obtained; conversely, as l decreases, only a smaller variation of θ distribution is found, but the trend is inverted.

3.2.2. Global parameters

The dependence of the friction factor f on l and L is shown in Fig. 17. Here, f is normalized by the value relevant to an empty channel, $24/Re$, and is reported as a function of L/l. As L/l increases, hydraulic friction is reduced and tends to attain the value relevant to the empty channel, both in the case of increasing pitch L and in the case of decreasing size l. For a given value of L/l, the absolute value of the two parameters has a negligible impact; in fact, the maximum discrepancy is just of 3%, obtained for $L/l = 2$. This confirms again the small importance of the L/h and l/h ratios.

When L/l decreases, an increasing rate of increment of the friction coefficient can be observed compared to the empty channel (up to +62% for the case *c-l1-L2-α45*), while it remains noticeably lower than that exhibited by the spacer-filled channel (~6.8·24/Re). Note that, for a fixed Re, the power number Pn defined by Eq. (10) is proportional to f as L/l varies so that it is not reported here.

Fig. 18 shows the dependence of the mean polarization factor θ_{ave} on L and l. As L/l varies, two different behaviours are found on the basis of the absolute value of L and l. For increasing L and fixed l, lower θ_{ave} values are obtained. Conversely, when l decreases

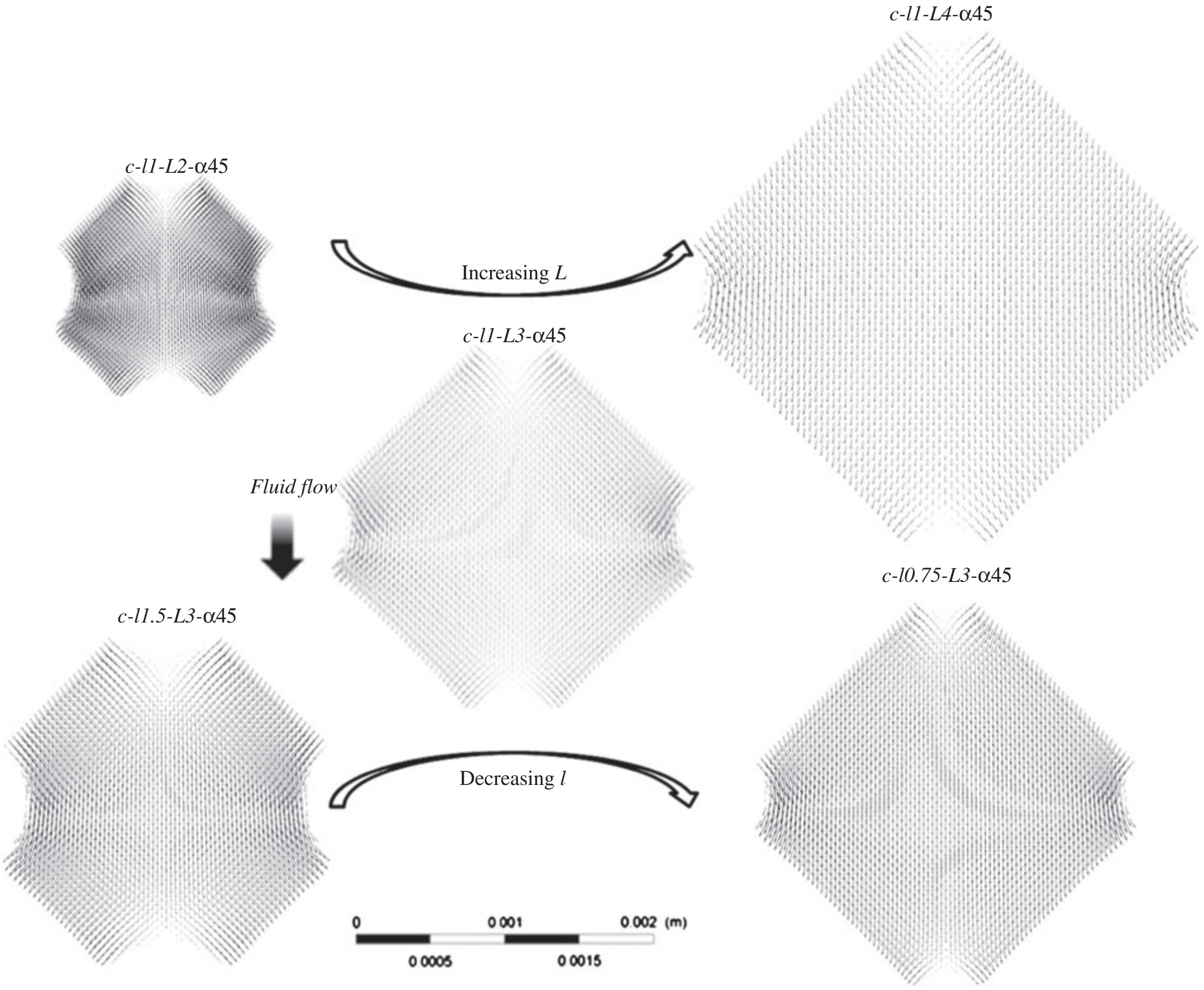

Fig. 15. Velocity vector plots on the x–z midplane for *c-l1-L2-α45*, *c-l1-L4-α45*, *l1–L3-α45*, *l1.5-L3-α45* and *l0.75-L3-α45* channels at $Re = 8$.

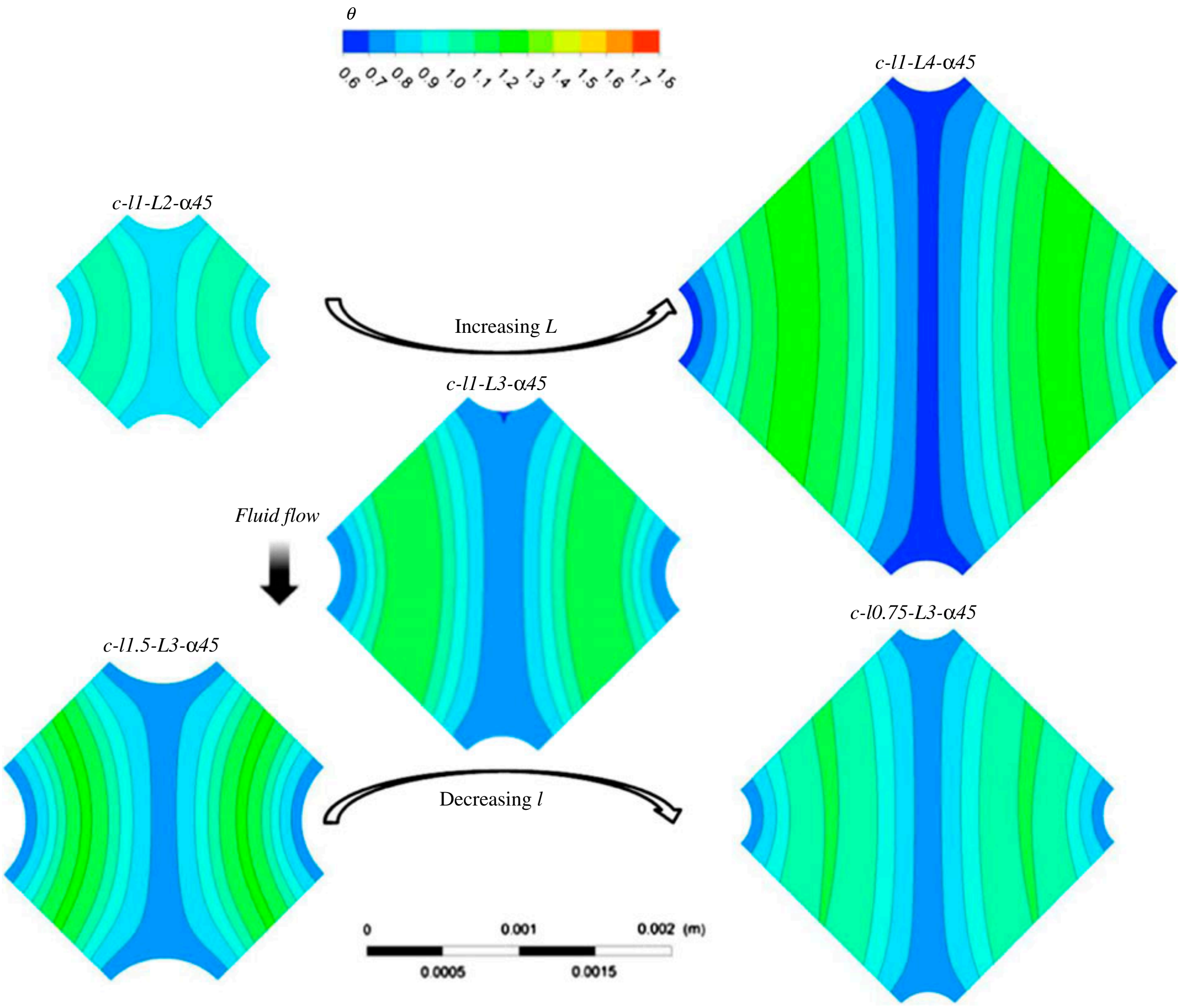

Fig. 16. Maps of the local polarization factor $\theta = \hat{C}_b / C_w$ on one of the fluid–membrane interfaces for *c-l1-L2-α45*, *c-l1-L4-α45*, *l1–L3-α45*, *l1.5-L3-α45* and *l0.75-L3-α45* channels at $Re = 8$.

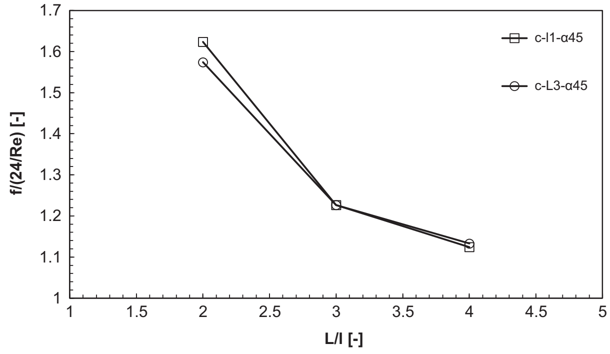

Fig. 17. Fanning friction factor normalized by that pertaining to an empty channel ($24/Re$) as a function of the profile pitch-to-size ratio for *c-α45* channels at $Re = 8$.

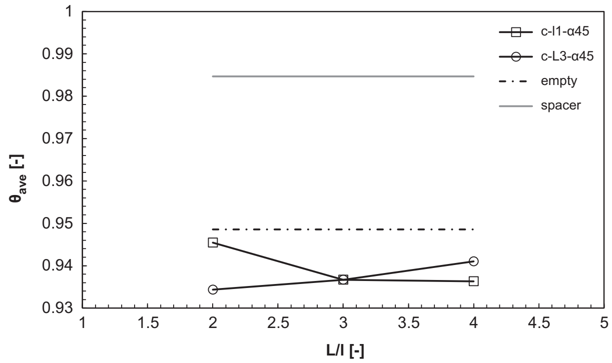

Fig. 18. Average polarization factor θ_{ave} as a function of the profile pitch-to-size ratio for *c-α45* channels at $Re = 8$. Empty and spacer-filled channels are also reported for comparison.

for a fixed L, θ_{ave} increases. Among the cases investigated, the maximum θ_{ave} is achieved for *c-l1-L2-α45* which is also the case of with the highest f (Fig. 17).

Clearly, a trend asymptotically approaching the θ_{ave} value of the empty channel is expected for $L/l \to \infty$. With respect to the spacer-filled channel, mixing remains less favoured for the present low *Re* (8); however, as shown by Figs. 12 and 13, values of θ_{ave} higher than in the empty channel are obtained for higher Reynolds numbers.

4. Conclusions

CFD simulations of channels with profiled membranes for RE, not yet investigated up to now, were carried out. The profiles were "pillars" that create the channels for the feed solutions. The effect of various parameters of the channel configuration on fluid flow and mass transfer was assessed. Velocity and concentration fields highlight the presence of calm zones of high polarization near the profiles and in the part of the channel comprised between two consecutive profiles along the main flow direction s. At low Reynolds numbers (*Re*) a creeping flow regime is present; as *Re* increases, inertial effects arise, thus causing a non-self-similarity of the flow field which, in its turn, (i) enhances the rate of increase of the pumping power consumption (*Pn*) with *Re* and (ii) favours mass transfer enhancement.

The flow attack angle α has an important role in determining velocity and concentration fields: the velocity distribution in a midplane parallel to the walls exhibits a saddle shape with features inverted from $\alpha = 0^\circ$ to $\alpha = 45^\circ$; a more uniform distribution of concentration is obtained in the case of $\alpha = 45^\circ$. With regard to the global parameters, it has practically irrelevant effects on *Pn*, especially for the circular profiles and low Reynolds numbers; also, higher average polarization factors θ_{ave} (lower polarization effects) are found in the case of the flow attack angle $\alpha = 45^\circ$ for both shapes.

The shape of the profiles is found to affect velocity and concentration fields very slightly, and an increment of 8% in *Pn* is caused by the square shape with respect to the circular one. Circular profiles give rise to a better mixing than square ones for $\alpha = 0^\circ$, while the influence of shape on polarization is minimal for $\alpha = 45^\circ$. Anyhow, at higher *Re* (≥32), a similar θ_{ave} is achieved regardless of shape and α.

A parametric analysis, focused on the effect of profile size l and pitch L in circular profiles and at $\alpha = 45^\circ$, shows that increasing L/l (2, 3, 4) leads to a less tortuous flow path, a more homogeneous velocity distribution, and a reduction of *Pn* with very similar effects caused both by the increase in L and by the decrease of l (i.e. less "filled" channel). On the contrary, the concentration field and the average polarization factor vary in a different way as a function of the two parameters L and l: as L increases (2, 3, 4 mm) with $l = 1$ mm, the local polarization field is less uniform and θ_{ave} decreases; as l decreases (1.5, 1, 0.75 mm) with $L = 3$ mm, a slightly more uniform θ distribution is found and θ_{ave} increases.

Profiled-membrane channels provide a power number *Pn* comparable with that relevant to the empty channel, (maximum increment ~62% for the configuration *c-l1-L2-α45*) in the range of the flow rates investigated. Mass transfer is disadvantaged by calm zones with high local polarization so that at low *Re*, θ_{ave} values even worse than that pertaining to the empty channel are obtained. However, beyond a cut-off value of *Re* ≈ 10–20, depending on the configuration, mixing is better than that offered by the empty channel, whose performance is independent of *Re*.

Compared to a high-performance net spacer-filled channel [2], *Pn* was found to be about five times lower in the profiled-membrane channels. On the other hand, mixing is improved by adopting a net spacer. Nevertheless, θ_{ave} values (of spacer-filled and profiled-membrane channels) tend to get closer at high *Re* and profiled-membrane channels promise to offer even better performance at higher *Pn*.

Finally, it should be stressed that the θ_{ave} values found in this work are quite close to 1 for seawater, but they can be much lower for more diluted solutions. In fact, polarization effects greatly increase as the solution bulk concentration decreases, becoming prominent for solutions as brackish or river water. Although the *difference* of concentration between bulk and membrane–solution interface is similar at various bulk concentrations (at a given current density), very different effects on the driving force can be obtained, quantified by the polarization factor which represents the *ratio* of bulk and interface concentration.

The optimal channel configuration could be identified by calculating the net power density producible by the stack, but various factors (e.g. residence time, electrical resistance, spacer shadow effect, etc.) should be taken into account, as well as pumping power consumption and polarization effects. However, the results of the present work confirm that the fundamental feature of channels generated by profiled membranes is a significant reduction of pumping costs with respect to spacer-filled channels. Also, suitable profiled-membrane geometry and Reynolds number can lead to a comparable reduction of polarization phenomena which, combined with advantages as lower electrical resistance, higher membrane active area and lower costs, makes the profiled-membrane channels a promising alternative for the optimization of the RE process. Finally, this study lays the groundwork for assessing performance of profiled-membrane channels, which offer endless geometric possibilities.

Acknowledgement

This work has been performed within the REAPower (Reverse Electrodialysis Alternative Power production) project, funded by the EU-FP7 programme (Project Number: 256736), http://www.reapower.eu.

Notations

a — slope of the function ρ *(C)* obtained via linear regression [kg mol^{-1}]
A — coefficient in Eq. (14) [–]
b — intercept of the function ρ *(C)* obtained via linear regression [kg m^{-3}]
B — coefficient in Eq. (15) [–]
C — molar concentration of electrolyte [mol m^{-3}]
$\tilde{C}$ — periodic molar concentration of electrolyte [mol m^{-3}]
$\hat{C}_b$ — bulk concentration of electrolyte [mol m^{-3}]
C_w — local molar concentration of electrolyte in the membrane–solution interfaces [mol m^{-3}]
$\overline{C}_w$ — mean molar concentration of electrolyte in the membrane–solution interfaces [mol m^{-3}]
D — measured diffusion coefficient of electrolyte [m^2 s^{-1}]
$d_{h,void}$ — hydraulic diameter of the spacer-less channel [m]
f — fanning friction factor [–]
F — Faraday's constant [C mol^{-1}]
h — channel thickness [m]
i — current density [A m^{-2}]
J_{IEM}^{d} — diffusive flux of electrolyte at the membrane–solution interface [mol m^{-2} s^{-1}]
$\overline{J}_{IEM}^{d}$ — mean diffusive flux at the membranes–solution interface [mol m^{-2} s^{-1}]
k — concentration gradient along the main flow direction [mol m^{-4}]
l — size of profiles [m]
L — pitch of profiles [m]
m — exponent to *Re* in Eq. (15) [–]
M_e — molar mass of electrolyte [kg mol^{-1}]
p — pressure [Pa]
$\tilde{p}$ — periodic component of pressure [Pa]
$\vec{P}$ — body force per unit volume [Pa m^{-1}]
Pn — power number
Re — Reynolds number [–]
s — main flow direction coordinate [m]
S_m — area of membrane–solution interfaces [m^2]
SPC — specific power consumption [Pa s^{-1}]
t — time [s]
$\vec{u}$ — velocity of solution [m s^{-1}]
u_s — velocity component along the direction s [m s^{-1}]
$u_{s,ave}$ — average velocity along the main flow direction s in the unit cell [m s^{-1}]
$u_{s,void}$ — average velocity along the main flow direction s in a corresponding spacer-less channel [ms^{-1}]
V — volume of a unit cell [m^3]
x — Cartesian position coordinate [m]
y — Cartesian position coordinate [m]
z — Cartesian position coordinate [m]
$\Delta p/\Delta s$ — mean pressure gradient along the main flow direction s [Pa m^{-1}]

Greek letters

α — flow attack angle [°]
θ — polarization factor
θ_{ave} — average polarization factor
μ — dynamic viscosity of solution [Pa s]
ρ — solution density [kg m^{-3}]

Abbreviations

CFD — computational fluid dynamics
ED — electrodialysis
IEM — ion-exchange membrane
RE — reverse electrodialysis

References

[1] P. Długołęcki, K. Nijmeijer, S.J. Metz, M. Wessling, Current status of ion exchange membranes for power generation from salinity gradients, J. Membr. Sci. 319 (2008) 214–222.

[2] L. Gurreri, A. Tamburini, A. Cipollina, G. Micale, M. Ciofalo, CFD prediction of concentration polarization phenomena in spacer-filled channels for reverse electrodialysis, J. Membr. Sci. 468 (2014) 133–148.

[3] R.E. Pattle, Production of elctric power by mixing fresh and salt water in hydroelectric pile, Nature 174 (1954) 660.

[4] J.W. Post, H.V.M. Hamelers, C.J.N. Buisman, Energy recovery from controlled mixing salt and fresh water with a reverse electrodialysis system, Environ. Sci. Technol. 42 (2008) 5785–5790.

[5] J. Veerman, M. Saakes, S.J. Metz, G.J. Harmsen, Reverse electrodialysis: Performance of a stack with 50 cells on the mixing of sea and river water, J. Membr. Sci. 327 (2009) 136–144.

[6] J. Veerman, M. Saakes, S.J. Metz, G.J. Harmsen, Reverse electrodialysis: A validated process model for design and optimization, Chem. Eng. J. 166 (2011) 256–268.

[7] D.A. Vermaas, E. Guler, M. Saakes, K. Nijmeijer, Theoretical power density from salinity gradients using reverse electrodialysis, Energy Procedia 20 (2012) 170–184.

[8] D.A. Vermaas, M. Saakes, K. Nijmeijer, Doubled power density from salinity gradients at reduced intermembrane distance, Environ. Sci. Technol. 45 (2011) 7089–7095.

[9] D.A. Vermaas, M. Saakes, K. Nijmeijer, Power generation using profiled membranes in reverse electrodialysis, J. Membr. Sci. 385–386 (2011) 234–242.

[10] V.I. Zabolotskii, S.A. Loza, M.V. Sharafan, Physicochemical properties of profiled heterogeneous ion-exchange membranes, Russ. J. Electrochem. 41 (2005) 1185–1192.

[11] K. Scott, J. Lobato, Mass transfer characteristics of cross-corrugated membranes, Desalination 146 (2002) 255–258.

[12] D.W. Hall, K. Scott, R.J.J. Jachuck, Determination of mass transfer coefficient of a cross-corrugated membrane reactor by the limiting-current technique, Int. J. Heat Mass Transfer 44 (2001) 2201–2207.

[13] V.V. Nikonenko, N.D. Pismenskaya, A.G. Istoshin, V.I. Zabolotsky, A.A. Shudrenko, Description of mass transfer characteristics of ED and EDI apparatuses by using the similarity theory and compartmentation method, Chem. Eng. Process. 47 (2008) 1118–1127.

[14] C. Larchet, V.I. Zabolotsky, N. Pismenskaya, V.V. Nikonenko, A. Tskhay, K. Tastanov, G. Pourcelly, Comparison of different ED stack conceptions when applied for drinking water production from brackish waters, Desalination 222 (2008) 489–496.

[15] J. Balster, D.F. Stamatialis, M. Wessling, Membrane with integrated spacer, J. Membr. Sci. 360 (2010) 185–189.

[16] H. Strathmann, Electrodialysis, a mature technology with a multitude of new applications, Desalination 264 (2010) 268–288.

[17] P. Długołęcki, J. Dąbrowska, K. Nijmeijer, M. Wessling, Ion conductive spacers for increased power generation in reverse electrodialysis, J. Membr. Sci. 347 (2010) 101–107.

[18] E. Brauns, Salinity gradient power by reverse electrodialysis: Effect of model parameters on electrical power output, Desalination 237 (2009) 378–391.

[19] D.A. Vermaas, D. Kunteng, M. Saakes, K. Nijmeijer, Fouling in reverse electrodialysis under natural conditions, Water Res. 47 (2013) 1289–1298.

[20] D.A. Vermaas, M. Saakes, K. Nijmeijer, Enhanced mixing in the diffusive boundary layer for energy generation in reverse electrodialysis, J. Membr. Sci. 453 (2014) 312–319.

[21] T. Adachi, S. Hasegawa, Transition of the flow in a symmetric channel with periodically expanded grooves, Chem. Eng. Sci. 61 (2006) 2721–2729.

[22] S. Eiamsa-ard, P. Promvonge, Numerical study on heat transfer of turbulent channel flow over periodic grooves, Int. Commun. Heat Mass Transfer 35 (2008) 844–852.

[23] H.A. Mohammed, A.N. Al-Shamani, J.M. Sheriff, Thermal and hydraulic characteristics of turbulent nanofluids flow in a rib-groove channel, Int. Commun. Heat Mass Transfer 39 (2012) 1584–1594.

[24] H. Wang, P. Iovenitti, E. Harvey, S. Masood, Numerical investigation of mixing in microchannels with patterned grooves, J. Micromech. Microeng. 13 (2003) 801–808.

[25] A.A.S. Bhagat, I. Papautsky, Enhancing particle dispersion in a passive planar micromixer using rectangular obstacles, J. Micromech. Microeng. 18 (2008) 085005.

[26] A.A.S. Bhagat, E.T.K. Peterson, I. Papautsky, A passive planar micromixer with obstructions for mixing at low Reynolds numbers, J. Micromech. Microeng. 17 (2007) 1017–1024.

[27] S.-S. Hsieh, Y.-C. Huang, Passive mixing in micro-channels with geometric variations through μPIV and μLIF measurements, J. Micromech. Microeng. 18 (2008) 065017.

[28] W. Jeon, C.B. Shin, Design and simulation of passive mixing in microfluidic systems with geometric variations, Chem. Eng. J. 152 (2009) 575–582.

[29] V. Kumar, M. Paraschivoiu, K.D.P. Nigam, Single-phase fluid flow and mixing in microchannels, Chem. Eng. Sci. 66 (2011) 1329–1373.

[30] M. Ciofalo, J. Stasiek, M.W. Collins, Investigation of flow and heat transfer in corrugated passages—II. Numerical simulations, Int. J. Heat Mass Transfer 39 (1996) 165–192.

[31] J.H. Doo, M.Y. Ha, J.K. Min, R. Stieger, A. Rolt, C. Son, Theoretical prediction of longitudinal heat conduction effect in cross-corrugated heat exchanger, Int. J. Heat Mass Transfer 55 (2012) 4129–4138.

[32] A.G. Kanaris, A.A. Mouza, S.V. Paras, Flow and heat transfer prediction in a corrugated plate heat exchanger using a CFD code, Chem. Eng. Technol. 29 (2006) 923–930.

[33] M.A. Mehrabian, R. Poulter, Hydrodynamics and thermal characteristics of corrugated channels: Computational approach, Appl. Math. Model. 24 (2000) 343–364.

[34] M. Ciofalo, I. Di Piazza, J. Stasiek, Investigation of flow and heat transfer in corrugated-undulated plate exchangers, Heat Mass Transfer 36 (2000) 449–462.

[35] L.Z. Zhang, Convective mass transport in cross-corrugated membrane exchangers, J. Membr. Sci. 260 (2005) 75–83.

[36] D.W. Green, R.H. Perry, Perry's Chemical Engineers' Handbook, 8th ed., McGraw-Hill, New York, NY, 2007.

[37] H. Ozbek, J.A. Fair, S.L. Phillips, Viscosity of Aqueous Sodium Chloride Solutions From 0 to 150°C, University of California, Berkeley, 2010.

[38] V. Vitagliano, P.A. Lyons, Diffusion coefficients for aqueous solutions of sodium chloride and barium chloride, J. Am. Chem. Soc. 78 (1956) 1549–1552.

[39] E. Brauns, Towards a worldwide sustainable and simultaneous large-scale production of renewable energy and potable water through salinity gradient power by combining reversed electrodialysis and solar power? Desalination 219 (2008) 312–323.

[40] E. Brauns, An alternative hybrid concept combining seawater desalination, solar energy and reverse electrodialysis for a sustainable production of sweet water and electrical energy, Desalin. Water Treat. 13 (2010) 53–62.

[41] M. Tedesco, A. Cipollina, A. Tamburini, G. Micale, J. Helsen, M. Papapetrou, Reapower—Use of desalination brine for power production through reverse electrodialysis, Desalin. Water Treat. (2014) doi: 10.1080/19443994.2014.934102.

[42] A. Tamburini, G. La Barbera, A. Cipollina, M. Ciofalo, G. Micale, CFD simulation of channels for direct and reverse electrodialysis, Desalin. Water Treat. 48 (2012) 370–389.

[43] L. Gurreri, A. Tamburini, A. Cipollina, G. Micale, CFD analysis of the fluid flow behavior in a reverse electrodialysis stack, Desalin. Water Treat. 48 (2012) 390–403.

[44] L. Gurreri, A. Tamburini, A. Cipollina, G. Micale, M. Ciofalo, CFD simulation of mass transfer phenomena in spacer filled channels for reverse electrodialysis applications, Chem. Eng. Trans. 32 (2013) 1879–1884.

[45] C.P. Koutsou, S.G. Yiantsios, A.J. Karabelas, Direct numerical simulation of flow in spacer-filled channels: Effect of spacer geometrical characteristics, J. Membr. Sci. 291 (2007) 53–69.

[46] Y.L. Li, K.L. Tung, CFD simulation of fluid flow through spacer-filled membrane module: Selecting suitable cell types for periodic boundary conditions, Desalination 233 (2008) 351–358.

[47] A. Tamburini, G. La Barbera, A. Cipollina, G. Micale, M. Ciofalo, CFD prediction of scalar tranport in thin channels for reverse electrodialysis, Desalin. Water Treat. (2014) accepted for publication.

[48] M. Shakaib, S.M.F. Hasani, M. Mahmood, CFD modeling for flow and mass transfer in spacer-obstructed membrane feed channels, J. Membr. Sci. 326 (2009) 270–284.

[49] G. Schock, A. Miquel, Mass transfer and pressure loss in spiral wound modules, Desalination 64 (1987) 339–352.

[50] F. Li, W. Meindersma, A.B. de Haan, T. Reith, Optimization of commercial net spacers in spiral wound membrane modules, J. Membr. Sci. 208 (2002) 289–302.